

Identifying Biomass Burning Emission Differences Between  $\text{NH}_3$   
& CO using 13 years of AIRS Satellite Measurements

Ashley A. Wheeler

A scholarly paper in partial fulfillment of the requirements for the degree of

Master of Science

December 2016

Department of Atmospheric and Oceanic Science, University of Maryland  
College Park, Maryland

Advisor: Dr. Juying Warner

## Table of Contents

**Acknowledgements**

**List of Tables**

**List of figures**

**List of symbols**

**Chapter 1. Introduction**

1.1 NASA Earth Observing System (EOS)

1.2 Aqua Satellite and AIRS Instrumentation

1.3 Atmospheric Ammonia; Importance, Modeling, and Satellite Observations

1.4 Atmospheric Carbon Monoxide; Importance and Satellite Observations

1.5 MODIS Fire Radiative Power

**Chapter 2. Data Sets & Methods**

2.1 Brief Retrieval Method Overview

2.2 Data Sets

2.3 Calculations

**Chapter 3. Results**

3.1 NH<sub>3</sub> and CO Global Distributions, Seasonal Correlation, & Relative Emissions Ratio

3.2 Identifying Fire Regions Using a “Threshold”

3.3 Regional Time Series of NH<sub>3</sub>, CO, and MODIS Total Fire Counts

**Chapter 4. Conclusions & Summary**

**References**

## **Acknowledgements**

I would like to thank my graduate advisor Dr. Juying Warner for her encouragement, support, and guidance throughout my academic career at the University of Maryland. Dr. Warner's passion for her research. It was a privilege to work with and learn from Dr. Warner, her enthusiasm for research is contagious.

I am forever thankful for the love and support of my parents, Anne and Brian Wheeler, and my brother Matthew. Without them I could not have made it this far. I would also like to thank my Grandfather, Fredrick Brooks, for inspiring me since a young age to love science and pursue big dreams. I would also like to thank the AOSC faculty and my fellow peers for enjoying this journey with me.

I am forever thankful for the love and support of my family. To my parents Anne and Brian Wheeler; Thank you for providing me with the opportunities that allowed me to reach this point as well as for your patience, reassurance, and understanding along the way. To my brother Matthew; Thank you for always believing in me and challenging me to be better. To my Grandfather Fredrick Brooks; Thank you for continuously inspiring me since a young age to love science and pursue big dreams. Without you all, I could not have made it this far.

Finally, thank you to all my friends, teammates, and coaches who have encouraged me to follow my passion. I am truly grateful for all those who have helped me and been a part of my career thus far.

Thank you!

Ashley

## List of Tables

### Table

1. Min/Max Latitude & Longitude Bounds of 6 Fire Regions

## List of Figures

### Figure

1. A-Train Satellite Configuration
2. IDL Example Code Demo. of “WHERE” Function Matching
3. AIRS 505mb CO VMRs for Each Season Averaged over 2003-2015
4. AIRS 918mb NH<sub>3</sub> VMRs for Each Season Averaged over 2003-2015
5. Multi-Panel Plot for Summer from 2003-2015  
*TOP LEFT: AIRS L2V6 500 mb CO VMR*  
*BOTTOM LEFT: AIRS L2V6 918 mb NH<sub>3</sub> VMR*  
*TOP RIGHT: NH<sub>3</sub> vs CO Correlation Coefficient*  
*BOTTOM RIGHT: NH<sub>3</sub> to CO Relative Emission Ratio*
6. Multi-Panel Plot for Spring from 2003-2015  
*TOP LEFT: AIRS L2V6 500 mb CO VMR*  
*BOTTOM LEFT: AIRS L2V6 918 mb NH<sub>3</sub> VMR*  
*TOP RIGHT: NH<sub>3</sub> vs CO Correlation Coefficient*  
*BOTTOM RIGHT: NH<sub>3</sub> to CO Relative Emission Ratio*
7. Screened Multi-Panel Plot for Summer from 2003-2015  
*TOP LEFT: MODIS Total Fire Counts*  
*BOTTOM LEFT: MODIS Fire Radiative Power*  
*TOP RIGHT: Screened NH<sub>3</sub> vs CO Correlation Coefficient.*  
*BOTTOM RIGHT: Screened NH<sub>3</sub> to CO Relative Emission Ratio*
8. Screened Multi-Panel Plot for Spring from 2003-2015  
*TOP LEFT: MODIS Total Fire Counts*  
*BOTTOM LEFT: MODIS Fire Radiative Power*  
*TOP RIGHT: Screened NH<sub>3</sub> vs CO Correlation Coefficient.*  
*BOTTOM RIGHT: Screened NH<sub>3</sub> to CO Relative Emission Ratio*

9. Map of 6 Fire Regions of Interest
- 10a. Regional Time Series of AIRS NH<sub>3</sub> and CO VMR with  
Total MODIS Fire Counts from 2003-2015  
*REGIONS: Africa North of Equator, Africa South of Equator  
Central South America, and South East Asia*
- 10b. Regional Time Series of AIRS NH<sub>3</sub> and CO VMR with  
Total MODIS Fire Counts from 2003-2015  
*REGIONS: Alaska/CA, Russia*

## List of Acronyms

AIRS	Atmospheric Infrared Sounder
EOS	Earth Observing System
ESE	Earth Science Enterprise
NASA	National Aeronautics and Space Administration
HCl	Hydrochloric Acid
HNO <sub>3</sub>	Nitric Acid
H <sub>2</sub> SO <sub>4</sub>	Sulfuric Acid
SOA	Secondary Organic Aerosols
MODIS	MODerate Resolution Imaging Spectroradiometer
FRP	Fire Radiative Power
mb	Millibar
NH <sub>3</sub>	Ammonia
CO	Carbon Monoxide
VMR	Volume Mixing Ratio
OE	Optimal Estimation

## **Chapter 1. Introduction**

### **1.1 NASA Earth Observing System (EOS)**

In the 1990s NASA's Earth Observing System (EOS) Program was founded as a part of the Earth Science Enterprise (ESE) in response to the growing recognition of societies impact on the natural variability and evolution of the planet. Following the discovery of the ozone hole over Antarctica, increasing carbon dioxide concentrations recorded at Mauna Loa, observed tropical deforestation, and global warming patterns predicted by climate models, there was a sense of urgency to understand the entire Earth system on a global scale. The overall goal of the EOS Program is "to advance the understanding of the entire Earth system on a global scale by improving our knowledge of the components of the system, the interactions between them, and how the Earth system is changing" (NASA, 1999). The EOS is composed of a series of coordinated polar-orbiting satellites producing long-term global observations used to understand critical aspects Earth's climate system, including; greenhouse gases, radiation, land and sea ice, clouds, ozone, the oceans, both natural and anthropogenic aerosols, precipitation, etc. As a part the Earth Science Division of NASA's Science Mission Directorate, the original EOS Program has been involved in international and multidisciplinary collaborations that lead to countless scientific discoveries studying the atmosphere, ocean, biosphere, cryosphere, land surface, and the relationships between them.

### **1.2 Aqua Satellite and AIRS Instrumentation**

Terra (formally AM-1) launched in 1999 as the first Earth Observing System satellite, collecting multiple types of data and becoming the first satellite to look at Earth system

science. Shortly following in 2002 was the launch Aqua (formerly EOS PM), the first of NASA's satellites that would make up the Afternoon Constellation or the A-Train. The A-train is a group of satellites overseen by NASA and international associates that closely follow each other in the same polar orbital track. Flying in a frozen sun-synchronous orbit, the satellites cross the equator at an altitude of roughly 705 km (Demarest et al., 2005). The six satellites currently in the A-Train: Orbiting Carbon Observatory (OCO-2), the Global Change Observation Mission-Water (GCOM-W1), Aqua, Cloud-Aerosol Lidar and Infrared Pathfinder Satellite Observation (CALIPSO), CloudSat, and Aura. See Figure 1 for illustration of A-Train satellite configuration.



**Figure 1.** The Afternoon Constellation (from right to left) OCO-2, GCOM-W1, Aqua, CALIPSO, CloudSat, and Aura.

The convoy formation of the six satellites allows for near-simultaneous measurements as they pass a given target within seconds to minutes within each other (Schoeberl et al., 2004). Multisensor observations from the satellites collectively produce a thorough vertical 3-D image of the atmosphere in various wavelengths and desirable climate parameters.

Aqua currently has 5 of its original six instruments working operationally: AIRS, AMSU, CERES, MODIS, and AMSR-E. For the purpose of this study, AIRS will be the primary instrument of interest.

The Atmospheric Infrared Sounder (AIRS) is cross-track scanning instrument designed to measure the water vapor content and temperature profiles of the Earth's atmosphere. The high spectral resolution grating spectrometer has 2378 bands in the thermal infrared from 3.7 to 15.4  $\mu\text{m}$  and 4 in the visible from 0.4 to 1.0  $\mu\text{m}$ . The spectral ranges have been precisely chosen in order for an accuracy of 1 K per 1 km thick layer in the troposphere for atmospheric temperature and 20% per 2 km thick layer in the lower troposphere for moisture profiles (Aumann et al., 2003). AIRS scans a  $\pm 49.5$  degree swath every 8/3 seconds, nadir and perpendicular to the flight path with 90 ground footprints per scan. Each individual footprint contains a single spectrum with all 2378 spectral samples taken simultaneously at a spatial resolution of 13.5 km (Aumann and Miller, 1995). Although designed as a meteorological mission, AIRS hyperspectral properties enable the retrievals for a number of atmospheric chemistry species or minor compositions.

### **1.3 Atmospheric Ammonia; Importance, Modeling, and Satellite Observations**

During recent years, the interest in atmospheric ammonia ( $\text{NH}_3$ ) has increased due to its role in global climate change and air quality, resulting in a range of studies. Ammonia is a critical component of the atmosphere composition and is an important factor in the acidification and eutrophication of ecosystems and determining the acidity of precipitation (Aneja et al., 2001, 2008; Shukla and Sharma, 2010). In its gaseous phase  $\text{NH}_3$  is one of the

only, and the most dominant, alkaline species in the atmosphere and neutralizes acidic species such as sulfuric acid ( $\text{H}_2\text{SO}_4$ ), hydrochloric acid ( $\text{HCl}$ ), and nitric acid ( $\text{HNO}_3$ ) into ammonium salts (Behera and Sharma, 2010). Secondary pollutants including  $\text{SO}_2$ ,  $\text{NO}_x$ , volatile organic compounds (VOCs), and ammonia are precursors to particulate matter (PM) formation which results in a significant portion of secondary particulate matter of diameter less than 2.5 micrometers, classified as  $\text{PM}_{2.5}$  (Behera and Sharma, 2010, 2012; Updyke et al., 2012). Fine particles are very concerning for human health because of their ability to penetrate deeper into lungs and the particle composition which can be very toxic. Compared to larger aerosols,  $\text{PM}_{2.5}$  particles remain suspended in the air for longer, travel further distances, and are capable of reaching indoor settings much easier due to their smaller size.  $\text{PM}_{2.5}$  has therefore been a chief index of PM exposure that is closely linked to cardiovascular and pulmonary health effects (Brook et al., 2010; Pope et al., 2011; Pope and Dockery, 2006). These ammonium nitrate and ammonium sulfate particles, formed through the reaction of  $\text{NH}_3$  with nitric acid and sulfuric acid, can also have a significant impact climate and the Earth's radiative balance. The effects occur; 1) directly by scattering and absorbing radiation, 2) indirectly by acting as cloud condensation nuclei (CCN) which impacts cloud formation and cloud radiative properties such as cloud albedo, and 3) contributes to absorption of solar radiation via formation of brown carbon through the reaction of  $\text{NH}_3$  with secondary organic aerosols (SOA) (Abbatt et al., 2006; Adams et al., 2001; IPCC, 2013; Langridge et al., 2012; Updyke et al., 2012).

Despite its importance  $\text{NH}_3$  is acknowledged as one of the most poorly quantified trace gases and is responsible for some of the largest uncertainties in reactive nitrogen

atmospheric transport (Fowler et al., 2013; Galloway et al., 2008; Pinder et al., 2006; Sutton et al., 2008). To understand better the magnitude, spatial, and seasonal variability of  $\text{NH}_3$  emissions models have been used to estimate atmospheric ammonia concentrations as well as atmospheric transport. However, it has been suggested that current models generally tend to underestimate concentration most particularly in the Northern Hemisphere which is largely industrialized (Heald et al., 2012). Globally there is a limited number of ground-based sites, networks, or field campaigns taking routine measurements of  $\text{NH}_3$  concentrations making it increasingly difficult to determine the spatial and temporal variability. Examples of such measurements include the US Ammonia Monitoring Network (AMoN), DISCOVER-AQ, and the European Monitoring and Evaluation Programme (EMEP). Even with sparse coverage the in-situ measurements can require expensive equipment and instruments that do not always prove to be reliable or consistent. Despite the increasing availability of airborne and ship campaign datasets, which provide important information about the vertical profile of  $\text{NH}_3$  and measurements over water respectively, these datasets only cover a short time period over small scales. Yet another downfall of in-situ measurements is the underrepresentation of the Southern Hemisphere which contains regions critical for understanding  $\text{NH}_3$  emissions on a global scale.

In contrast to other techniques, satellite remote sensing provides high spatial and temporal resolution that can complement and filling the gap left by in-situ measurements. The first satellite observations of lower tropospheric  $\text{NH}_3$  were made over Beijing, China using the Tropospheric Emission Spectrometer (TES) aboard the Aura satellite (Beer et al., 2008). The TES  $\text{NH}_3$  retrieval strategy was thoroughly explained by Shephard et al. (2011) who

concluded that TES retrievals are primarily sensitive to  $\text{NH}_3$  between 700 and 900 mb and produced global maps from TES  $\text{NH}_3$ . Utilizing their findings, Luo et al. (2015) investigated the seasonal and global distributions and correlations of  $\text{NH}_3$  to CO from TES satellite observations compared to GEOS-Chem model simulations for 2007 (Bey et al., 2001). Ammonia was detected inside biomass burning plumes during August 2007 in Greece within a spectra from the Infrared Atmospheric Sounder Interferometer (IASI) aboard the European MetOP polar orbiting satellites (Coheur et al., 2009). Observations from IASI enabled global daily monitoring due to a quick retrieval method, constructed around calculation total column measurements from brightness temperature, leading to the first global map of  $\text{NH}_3$  distributions (Clarisse et al., 2009). During a case study of the San Joaquin Valley Clarisse et al. (2010) focused on the sensitivity and ability of infrared instruments to probe the lower troposphere. Using a more refined algorithm they determined that the peak sensitivity for  $\text{NH}_3$  is within the boundary layer and can be measured in cases when thermal contrast is large between the surface and bottom of the atmosphere and  $\text{NH}_3$  concentrations are high (Clarisse et al., 2010). Clarisse et al. (2010) also examined instrument and measurement sensitivity for daytime versus nighttime as well as for different seasons. Following this study the  $\text{NH}_3$  detection sensitivity and retrieval from IASI has been continually improved, first by Walker et al. (2011) and then by Van Damme et al. (2014, 2015). Shephard and Cady-Pereira (2015) have also observed atmospheric  $\text{NH}_3$  using the Cross-track Infrared Sounder (CrIS) on the Suomi National Polar-orbiting Partnership (NPP) satellite.

While the studies mentioned above have made immense contributions to furthering our knowledge of the seasonal variation and spatial distribution of  $\text{NH}_3$  emissions large uncertainties still exist. In a most recent study Warner et al. (2016) describes a new  $\text{NH}_3$  retrieval method for the Atmospheric Infrared Sounder (AIRS) aboard NASA's EOS Aqua satellite, producing a daily and global ammonia product spanning 14 years from September 2002 to August 2016. The dataset presented by Warner et al. (2016) is the longest  $\text{NH}_3$  record to date and will be critical to advancing our understanding of  $\text{NH}_3$  emissions as well as the global nitrogen cycle. The 14-year dataset provided by Warner et al. (2016) was used for the purposes of this study, and will be described in greater detail in "Chapter 2: Data Sets & Methods" and for the remainder of the paper.

#### **1.4 Atmospheric Carbon Monoxide: Importance and Satellite Observations**

Since 2002 AIRS has been making global measurements of carbon monoxide (CO). Other sensors have contributed to global CO measurements such as; the Measurement Of Pollution In The Troposphere (MOPITT), the Tropospheric Emission Spectrometer (TES), the Infrared Atmospheric Sounder Interferometer (IASI), and The Cross-track Infrared Sensor (CrIS). It is critical to understand CO in the atmosphere since it has both direct and indirect impact and can be oxidized to form carbon dioxide ( $\text{CO}_2$ ), a vital greenhouse gas. Due to its tropospheric lifetime of around 1-3 months, CO can have effects at larger scales and be used as a tracer for atmospheric motions (Badr and Probert, 1994). Global measurements of CO are essential for atmospheric chemistry models and air quality health assessments due to its influences as a major sink for hydroxyl (OH) and precursor for

tropospheric ozone and smog (Crutzen et al., 1979). It is also important to note that emissions of CO from biomass burning challenges its anthropogenic emissions at 50/50 and causes most of its interannually variability (van der Werf et al., 2006). For the purpose of this study, CO and NH<sub>3</sub> have overlapping emission sources from biomass burning including wildfires and agricultural fires (Akagi et al., 2011) which will aid in determining origins of the observed NH<sub>3</sub> measurements.

## **1.5 MODIS Fire Radiative Power**

The active fire products produced by NASA's Moderate Resolution Imaging Spectroradiometer (MODIS) provide important information that has been used in countless biomass burning studies (Giglio et al., 2006; Justice et al., 2002). The active fires are monitored and detected at a resolution of about 1 km using the 4  $\mu\text{m}$  and 11  $\mu\text{m}$  bands to derive brightness temperatures (Justice et al., 2002). Fire Radiative Power (FRP), which is derived from the 4  $\mu\text{m}$  band, is the rate at which the actively burning fire is emitting radiative energy, at the time of observation, expressed in units of power (Js<sup>-1</sup> or Watts). Wooster et al. (2005) linked FRP to combustion rate by showing the linear relationship between the amount of biomass burned in a fire and the radiation released by the fire. From this concept, we can use FRP to identify biomass burning regions and analyze NH<sub>3</sub> and CO emission ratios.

## Chapter 2. Data Sets & Methods

### 2.1 Brief Retrieval Method Overview

The 13 year data set used during this study, spanning from 2003 through 2015, was produced by a retrieval algorithm using an optimal estimation (OE) technique that was developed by Warner et al. (2016). This AIRS NH<sub>3</sub> retrieval algorithm was based off AIRS carbon monoxide (CO) products established by Warner et al. (2010) and expanded off the current AIRS operational system algorithm (Susskind et al., 2003) with the exception of an alternate minimization method. It is important to note that AIRS data coverage has been increased from pure clear the coverage of about 10-15%, to roughly 50-70% of total measurements at 13.5 km<sup>2</sup> for a single pixel (Warner et al., 2013) as a result of AIRS cloud clearing capabilities outlined in Susskind et al. (2003). To ensure the greatest sensitivity to NH<sub>3</sub>, the retrievals were completed at 12 channels of AIRS radiances within the window regions of 860-875, 928-932, and 965-967 cm<sup>-1</sup>.

For a more thorough and detailed account of the AIRS NH<sub>3</sub> retrieval method please refer to Warner et al. (2016).

### 2.2 Data Sets

This study exams various data sets over the time period of 13 years from 2002-2015. Both the carbon monoxide and ammonia data sets used during this study were retrieved and provided by Dr. Juying Warner using AIRS Level 2 Version 6 and OE method. The CO data was provided in daily swath (240 granules per day) Hierarchical Data Format (HDF) files (Warner et al., 2010), from which CO VMR at 505 mb was extracted. The NH<sub>3</sub> VMR data was obtained at 918 mb from daily Network Common Data Form (NetCDF) files

(Warner et al., 2016). As the AIRS NH<sub>3</sub> was being read in, it was also screened to ensure only the highest quality data with elevated emissions (NH<sub>3</sub> VMR  $\geq$  1.0 ppbv) was kept. The screening criteria includes;

1. AIRS CCR quality assurance flag = Q0 (Highest quality)
2. The degrees of freedom for signal (DOFS) provided by the OE retrieval output must be  $\geq$  0.1 as to eliminate noise and keep the data where AIRS sensitivity is high.
3. From the minimization procedure outlined in Warner et al. (2016),  $\chi^2$ , must be greater than 0.9 and less than 27.0
4. Retrieval residual < 1 K
5. Solar zenith angle < 90°
6. Use only cases over land; land-fraction  $\geq$  0.8

Note that NH<sub>3</sub> VMR is being used at the selected level of 918 mb for a specific reason. In the lowest level of the atmosphere between 850 mb and the surface, the AIRS retrievals are sensitive to NH<sub>3</sub>. At around 918 mb this sensitivity peaks (Warner et al., 2016). As a result, areas with elevations higher than 918 mb may consequently contain missing data. Regions characterized as having persistent cloudy days will additionally contribute to missing data. It is also important to note that for both the AIRS NH<sub>3</sub> and AIRS CO each valid pixel over the day-is kept. This means that for each pixel the granule ID and pixel ID will need to be recorded for the matching process to be described in Section 2.3.

To support analysis, Global Monthly Fire Location Collection 6 Standard Product (MCD14ML) from the MODerate Resolution Imaging Spectroradiometer (MODIS)

instrument was used to acquire Fire Radiative Power (FRP) and Total Fire Counts information (Giglio, 2015; Giglio et al., 2016; Justice et al., 2002).

## 2.3 Calculations

First, daily CO data files must be compiled by reading in individual AIRS CO granule (swath) HDF files into a new daily ASCII file containing the necessary data for all 240 granules over a given day. AIRS NH<sub>3</sub> data coverage has been restricted to only over land as specified in section 2.2 above, while AIRS CO measurements cover the entire globe.

Therefore, in order to carry out calculations between NH<sub>3</sub> and CO and compare relative concentrations, we can only use the data where both the NH<sub>3</sub> and CO data sets have valid pixels. In this instance, a “valid pixel” is being defined as a case during a day where a given pixel-granule combination is mutually present in the daily NH<sub>3</sub> and CO data sets. By “matching” the two sets of data we are verifying that the data used will hold the same number of daily VMR pixels for NH<sub>3</sub> and CO, and each NH<sub>3</sub> pixel will have a CO pixel counterpart that were measured on the AIRS simultaneously at the same latitude/longitude location. Note; when investigating a given time period other than a day such as months, seasons, years, and seasons over the 13-year data set, each individual valid daily pixel within the time range will be kept as opposed to averaging over a grid. Accumulating all valid daily pixels within the investigated period proved to greatly improve the correlation between NH<sub>3</sub> and CO compared to that from 1° x 1° grid binned and averaged VMRs.

NH<sub>3</sub> to CO correlation coefficients and NH<sub>3</sub>/CO VMR ratios were calculated within 2.5° x 2.5° latitude longitude degree grid. Via a simple gridding or “binning” process written in IDL; for each 2.5° x 2.5° grid box, corresponding NH<sub>3</sub> and CO pixel data within the

min/max latitude and longitude range was located using IDL's built in "WHERE" function (<http://www.harrisgeospatial.com/docs/WHERE.html>). The following is example code demonstrating the use of the "WHERE" function and rational operator expressions within "FOR-loops" to bin NH<sub>3</sub> and CO data into a 2.5° x 2.5° grid;

```

numLAT = 72          ; 180 / 2.5 >>> 180 FOR 1X1
numLON = 144         ; 360 / 2.5 >>> 360 FOR 1X1

FOR y_grid = 0,numLAT -1 DO BEGIN          ; LATITUDE LOOP
  LATnxt = 2.5*y_grid
  FOR x = 0,numLON-1 DO BEGIN              ; LONGITUDE LOOP
    LONnxt = 2.5*x

;***** DETERMINE CURRENT START & END LATITUDE
    Slat = -90.0 + LATnxt
    Elat = Slat + 2.5

;***** DETERMINE CURRENT START & END LONGITUDE
    Slon = -180.0 + LONnxt
    Elon = Slon + 2.5

; RETURNS INDEX ARRAY FOR WHERE LAT/LON COMBO IS VALID , !NULL IF NOT
I_grid = WHERE(((pixLAT gt Slat) AND (pixLAT lt Elat)) AND $
              ((pixLON gt Slon) AND (pixLON lt Elon)) , /NULL)
; ^^^ RETURNS "NULL"
; INSTEAD OF "-1" WHEN
; NO DATA FOUND IN
; LAT/LON COMBO

;***** CHECK/REQUIRE 5 MATCHED PIXELS TO CONTINUE AND CALCULATE
; CORRELATION COEFFICIENT AND NH3/CO RATIO
IF (N_ELEMENTS(I_grid) gt 5) THEN BEGIN

;-----> USE "I_grid" INDEX TO GET CURRENT GRID BOX "COvmr" & "NH3vmr" VALS
NH3_25x25 = NH3vmr[I_grid]
CO_25x25 = COvmr[I_grid]

```

**Figure 2.** IDL Example Code Demonstrating using the built in IDL "WHERE" function to match AIRS L2V6 NH<sub>3</sub> and CO daily pixel-ID and granule-ID data matching

Where “pixLAT” and “pixLON” are, arrays containing the respective latitude and longitude coordinates for the corresponding pixel VMR values in arrays “NH3vmr” and “COvmr”. The center latitude and longitude of the grid box can be determined by adding  $1.25^\circ$  to the current values for starting latitude (“Slat”) and starting longitude (“Slon”). It is necessary to calculate and record the center latitude and longitude for plotting the correlation and ratio data on a map.

After the valid data for a  $2.5^\circ \times 2.5^\circ$  has been located and checked for missing/invalid data (ie -999.00 fill values), the NH<sub>3</sub>:CO ratio is calculated first by summing the VMRs values within the grid box NH<sub>3</sub> and CO arrays and then dividing the total of NH<sub>3</sub> by the total of CO. To compute the NH<sub>3</sub> vs CO correlation coefficient, the IDL built in function “CORRELATE” was used (<https://www.harrisgeospatial.com/docs/correlate.html>). The “CORRELATE” function calculates the linear Pearson correlation coefficient from two vectors, which in this case is the individual  $2.5^\circ \times 2.5^\circ$  grid box NH<sub>3</sub> and CO VMR arrays. If two arrays of different lengths are correlated with this function, only the data up to the last index of the smaller array will be used for both vectors. This highlights another reason why it is critical that the NH<sub>3</sub> and CO data are matched by daily pixel and granule ID, so that only data where both NH<sub>3</sub> and CO measurements exist and are valid (i.e. no -999.00) are used.

## Chapter 3. Results

### 3.1 NH<sub>3</sub> and CO Global Distributions, Seasonal Correlation, and Relative Emissions Ratio

The primary motivation of this study is to explore the relationship between NH<sub>3</sub> and CO concentrations in hopes of using this knowledge and information to identify fire emission differences for; various regions of the planet (high vs low latitude), over diverse vegetation/land types, and how these emission differences change depending on the season and over the course of the 13 years of data. I will first be examining the global distributions of NH<sub>3</sub> and CO for all four seasons over 2003-2015 designated as; DJF (December, January, February), MAM (March, April, May), JJA (June, July, August) and SON (September, October, November). During this study season names; Winter, Spring, Summer, and Fall are used in reference to the Northern Hemisphere (NH).

Figure 3 and Figure 4 show the global distribution maps for AIRS CO VMR and AIRS NH<sub>3</sub> VMR, respectively, for the four seasons over the 13-year period. As seen from Figure 3, CO VMR is lower in northern hemisphere Summer and Fall due to increase photochemical processes resulting from increased plant growth while it is much higher in the Winter and Spring months due to lack of plant growth and therefore CO accumulates. In Figure 4, the differences in NH<sub>3</sub> VMR between the four seasons can mostly be attributed to changes biomass burning and fertilizer applications and animal feeding from season to season.

# AIRS 505mb CO VMR ( $1^{\circ} \times 1^{\circ}$ ) 2003-2015

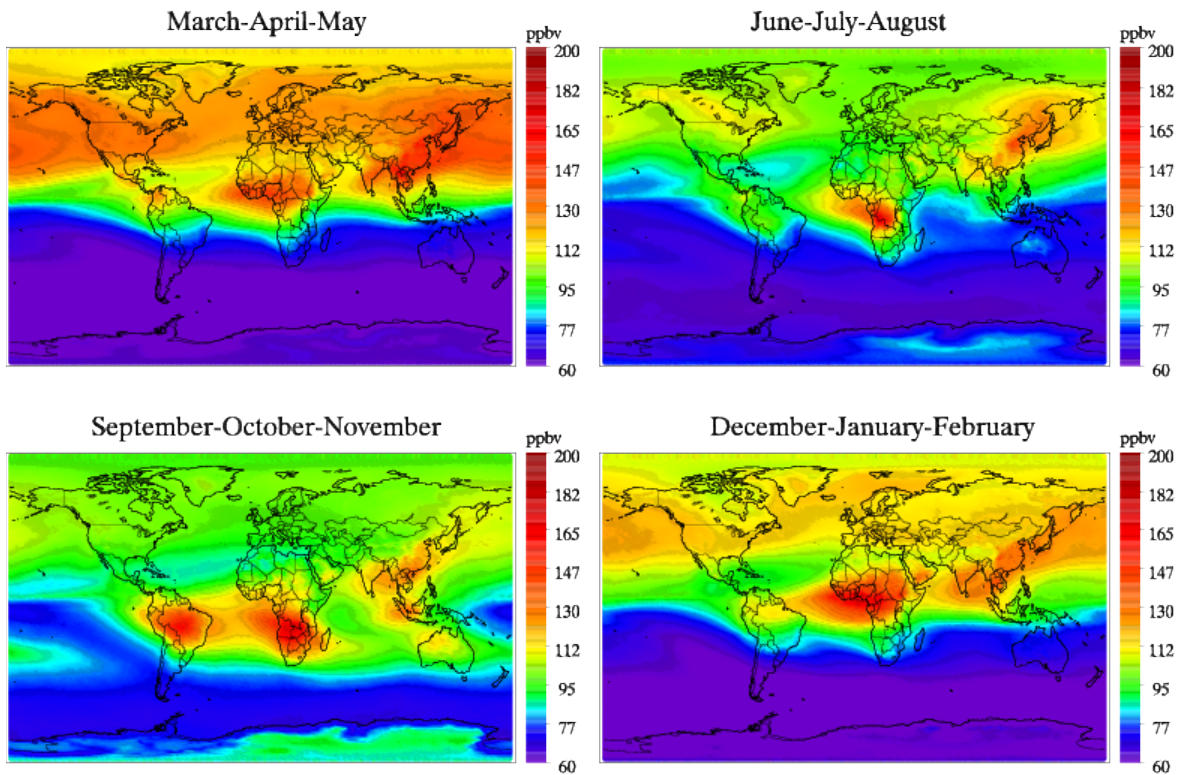


**Figure 3.** Multi-Panel Plot of AIRS 505mb CO VMRs Averaged over 2003-2015 for Each Season. March-April-May (top left), June-July-August (bottom left), September-October-November (top right), December-January-February (bottom right).

## AIRS 918mb NH<sub>3</sub> VMR (1°x1°) 2003-2015

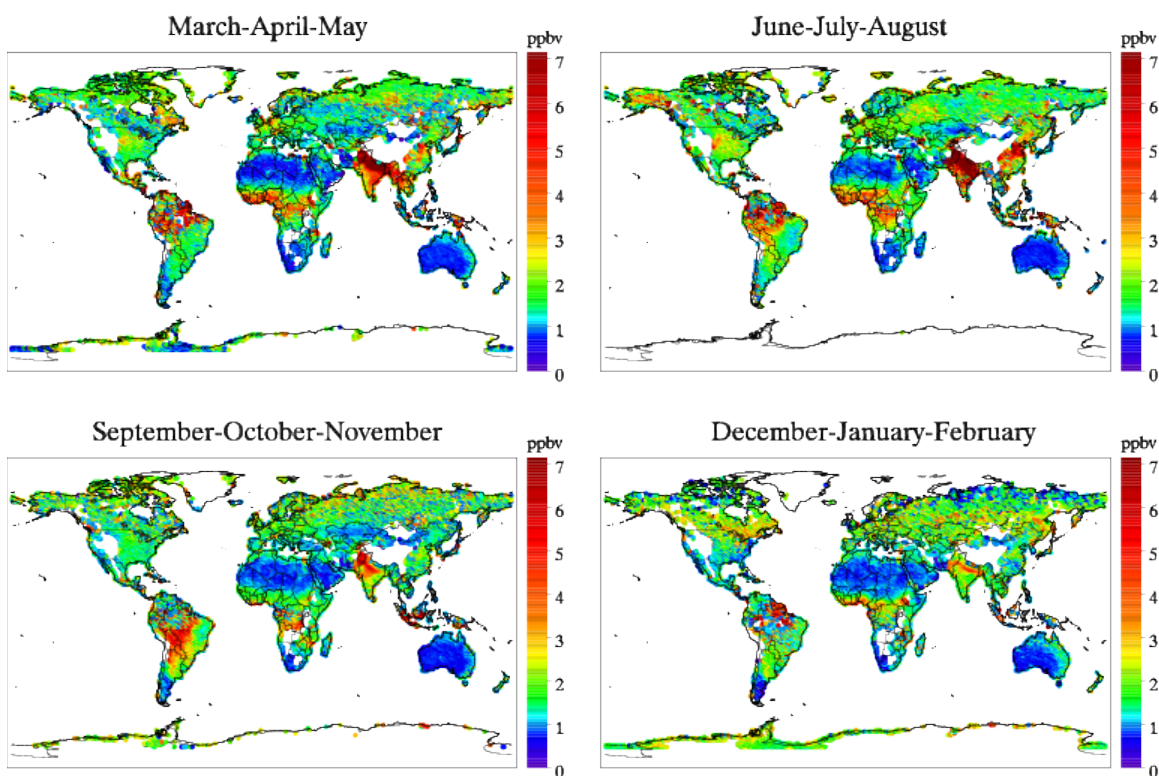


**Figure 4.** Multi-Panel Plot of AIRS 918mb NH<sub>3</sub> VMRs Averaged over 2003-2015 for Each Season. March-April-May (top left), June-July-August (bottom left), September-October-November (top right), December-January-February (bottom right).

To examine the relationship between emissions of NH<sub>3</sub> and CO, we will take a closer look at the northern hemisphere Spring and Summer seasons. Figure 5 and Figure 6 show the NH<sub>3</sub> vs CO correlation coefficient calculated within each 2.5°x2.5° grid box for Summer and Spring (respectively) during 2003-2015. In the top right panel green (purple) 2.5°x2.5° boxes indicate positive (negative) correlation NH<sub>3</sub> vs CO, and in the bottom right panel dark red (pink-red) 2.5°x2.5° boxes indicate high (low) NH<sub>3</sub>/CO ratio. Regions where correlation is positive and relative ratio also high suggest that more NH<sub>3</sub> is being produced relative to CO, which is likely from biomass burning. Therefore, the strong correlation seen

in Figure 5 over Alaska and Russia during NH Summer can be categorized as biomass burning regions, which are most likely due to sporadic wildfire events. Furthermore, the high  $\text{NH}_3/\text{CO}$  ratio also within these regions may hint that the vegetation and/or soil at higher latitudes release more  $\text{NH}_3$  relative to CO than in tropical regions. During NH Spring background CO concentrations have built up over the winter due to increased lifetime (decreased sinks), resulting in large emission and source differences compared to  $\text{NH}_3$ . Such cases can be seen from Figure 6; where correlation is negative, indicated by purple squares, and the relative emission  $\text{NH}_3$  is higher than CO which generally indicates a non-biomass burning region (agriculture or industrial sites).

Regions such as North-Central China and South-Central Asia where  $\text{NH}_3$  and CO are very strongly correlated for the majority of the year, but are also characterized as highly populated, industrialized, and also have seasonal agriculture practices are difficult to understand since they have mixed sources. These type of regions (and/or seasons) present conflicting positive/negative correlation and high/low relative VMR ratio cases, and thus cannot be designated as either a biomass burning or anthropogenic dominated region/season. As a result of these uncategorized “mixed source” cases it not reasonable to identify global fire regions solely by high  $\text{NH}_3$  vs CO correlations. Therefore, a “threshold” value may be determined to help locate/pinpoint a separation between; biomass burning dominating high  $\text{NH}_3$  and CO regions, from anthropogenic dominating high  $\text{NH}_3$  regions. This concept will be further discussed in the next “Section 3.2 Identifying Fire Regions Using a ‘Threshold’”, where a preliminary “threshold” value will be proposed to locate fire regions in addition to strong correlation.

# Summer 2003-2015

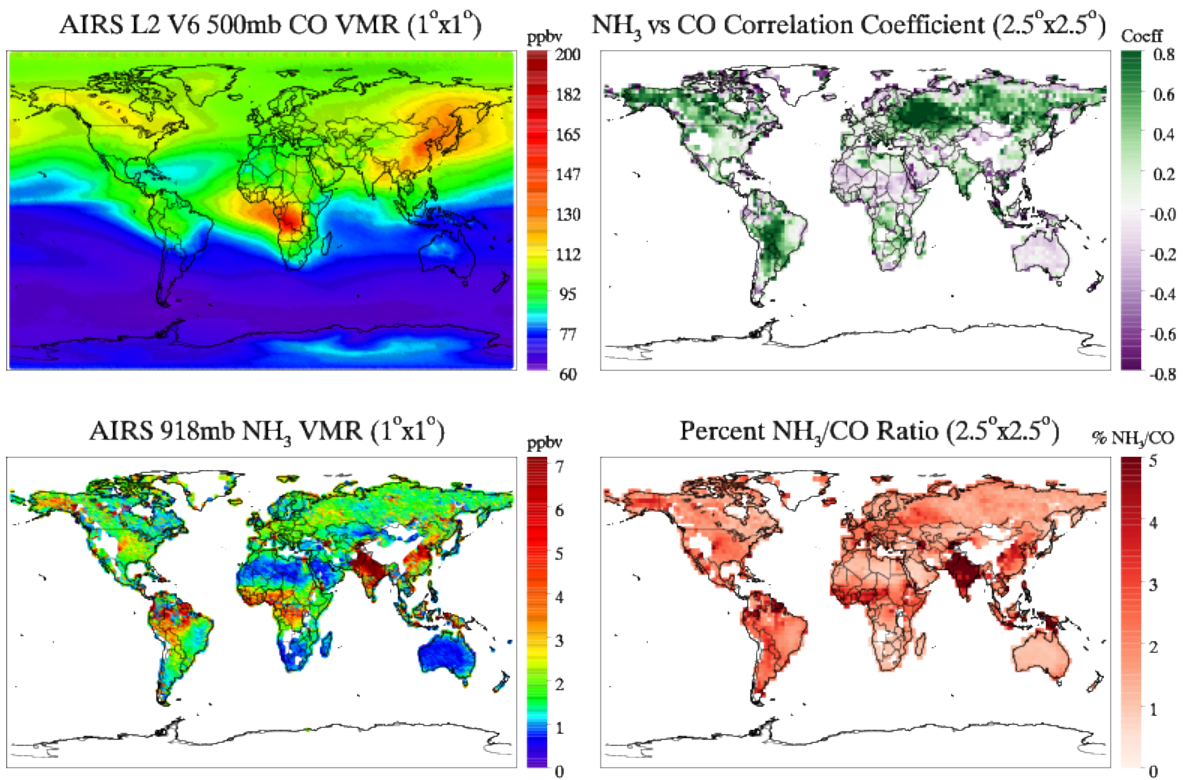


**Figure 5.** Multi-Panel Plot for Summer from 2003-2015. AIRS 500 mb CO VMR (top left), AIRS 918 mb NH<sub>3</sub> VMR (bottom left), NH<sub>3</sub> vs CO Correlation Coefficient (top right), NH<sub>3</sub> to CO Relative Ratio (bottom right).

# Spring 2003-2015

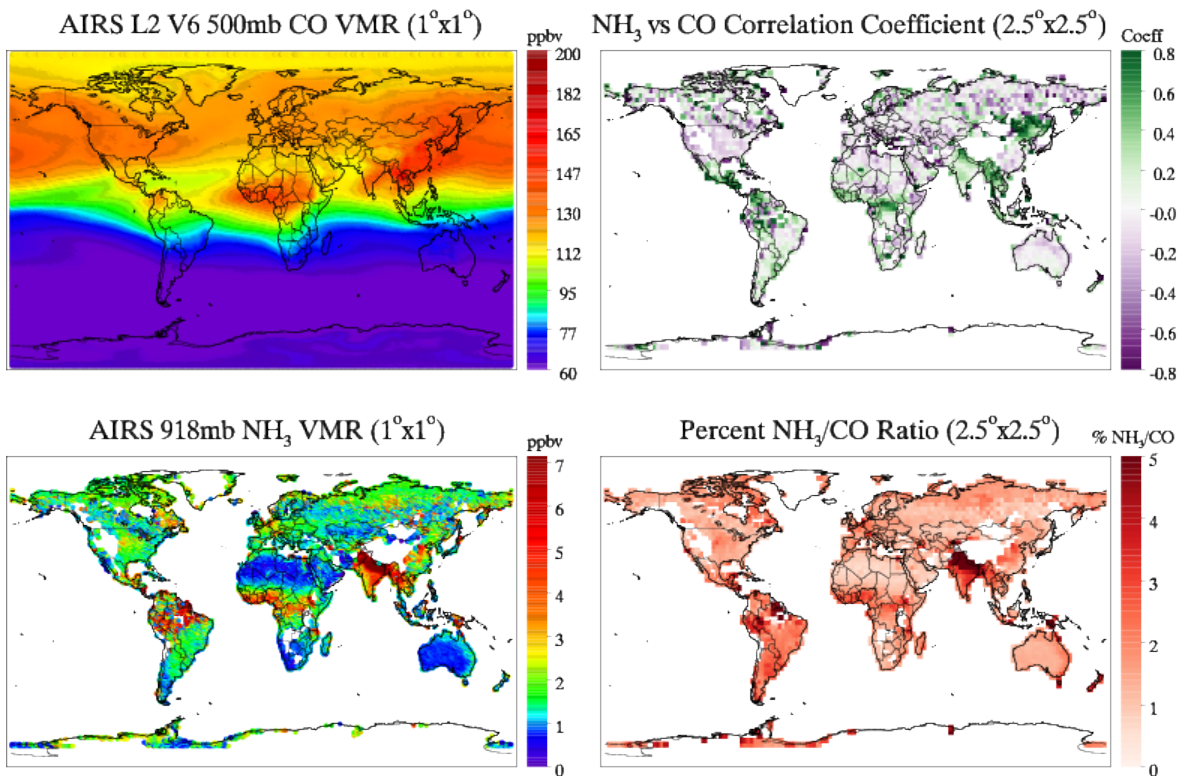


**Figure 6.** Multi-Panel Plot for Spring from 2003-2015. AIRS 500 mb CO VMR (top left), AIRS 918 mb NH<sub>3</sub> VMR (bottom left), NH<sub>3</sub> vs CO Correlation Coefficient (top right), NH<sub>3</sub> to CO Relative Ratio (bottom right).

## 3.2 Identifying Fire Regions Using a “Threshold”

During this Section, a MODIS Global Monthly Fire Location Product will be used to assist and advance the understanding of the emission differences between NH<sub>3</sub> and CO outlined in the previous Section. The addition of MODIS Average FRP and Total Fire Count data will support the current analysis through validation in choosing a “threshold” value. The “threshold” selected is intended to be used coupled with NH<sub>3</sub> vs CO correlation coefficients to better identify and constrain critical fire regions. After testing multiple options the “threshold” of where NH<sub>3</sub> vs CO correlation coefficient > 0.6 was selected.

# Summer 2003-2015

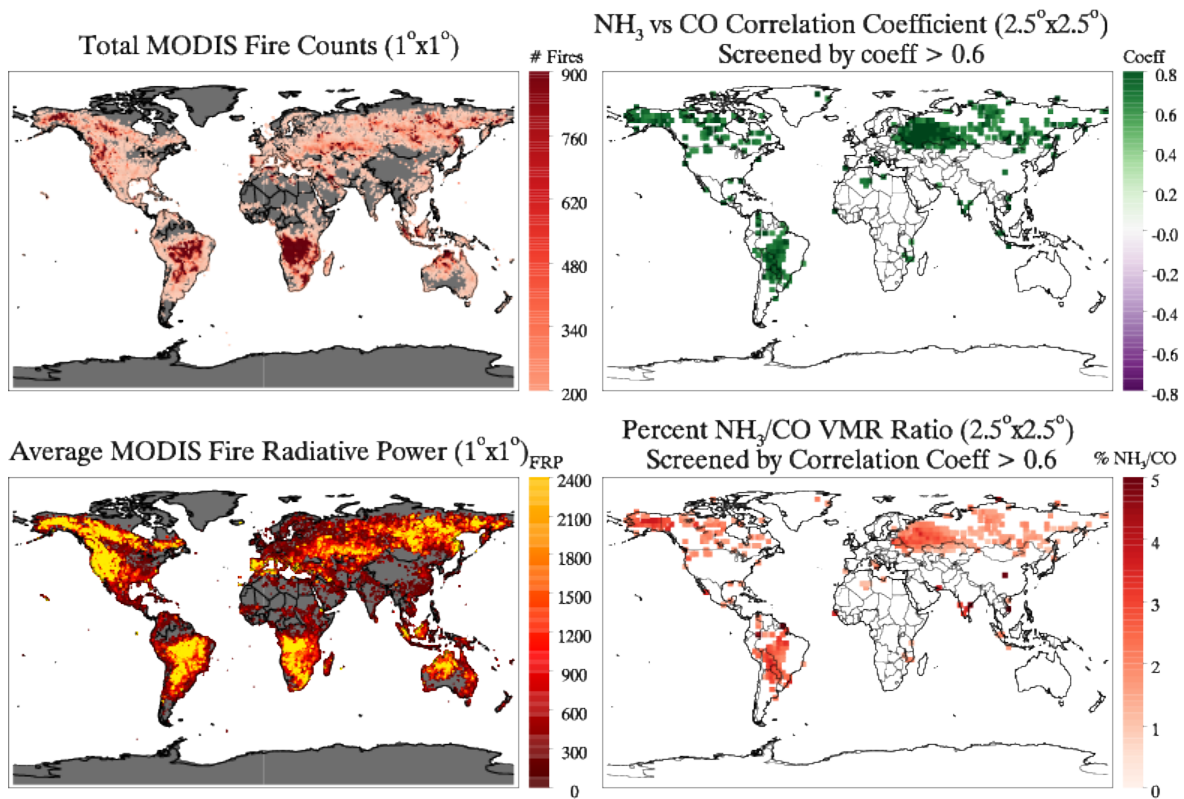


**Figure 7.** Screened Multi-Panel Plot for Summer from 2003-2015. MODIS Total Fire Counts (bottom left), MODIS FRP (top left), Screened NH<sub>3</sub> vs CO Correlation Coefficient (top right), Screened NH<sub>3</sub> to CO Relative Ratio (bottom right). Screened where NH<sub>3</sub> vs CO Correlation Coefficient > 0.6.

# Spring 2003-2015

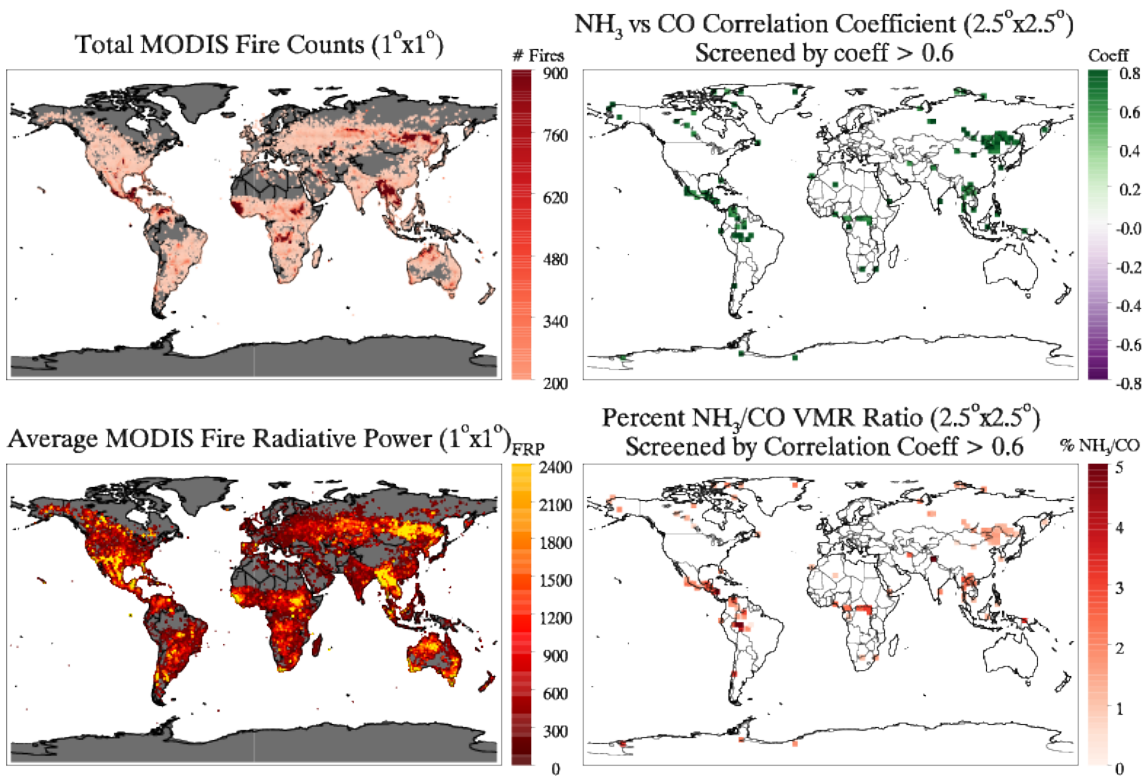


**Figure 8.** Screened Multi-Panel Plot for Spring from 2003-2015. MODIS Total Fire Counts (bottom left), MODIS FRP (top left), Screened  $\text{NH}_3$  vs CO Correlation Coefficient (top right), Screened  $\text{NH}_3$  to CO Relative Ratio (bottom right). Screened where  $\text{NH}_3$  vs CO Correlation Coefficient  $> 0.6$ .

Figure 7 and Figure 8 above, for the NH Summer and Spring seasons (respectively) over the entire 13-year data set, displays  $\text{NH}_3$  vs CO correlation coefficients and  $\text{NH}_3$  to CO ratios screened by the “threshold” value. More specifically, the data used for the two right panel maps was plotted in only the  $2.5^\circ \times 2.5^\circ$  grid boxes where the correlation coefficient was calculated to be greater than 0.6. The resulting number of grid boxes meeting the “threshold” criteria is much greater for NH Summer compared to NH Spring, as shown in Figures 7 and 8. These two plots allow for the relative emission ratio, which was screened to represent the theoretical fire regions, to be compared against actual MODIS fire location data for validation.

For NH Summer the highest values for MODIS Total Fire Counts and average FRP, indicated by dark red and bright yellow respectively, match well to the screened data locations on the right panel. In addition to being reoccurring seasonal wild fire regions, the stand out hot spots over Russia, Alaska and South America are the result of very large fires that occurred over the years 2009-2011, specifically in these regions, producing high  $\text{NH}_3$  concentrations for weeks (R'Honi et al., 2013). As an initial assessment, this indicate that 0.6 is relatively successful (except for a few areas such as Southern Africa) at selecting important fire region. It is important to note that in some instances areas that are showing “no data” for  $\text{NH}_3$  and CO, particularly Southern Africa for example, may be due to retrieval difficulties and therefore lacking representation in those areas. Despite the smaller number of grids containing correlation coefficient greater than 0.6, the NH Spring hot spots designated by MODIS fire data still match relatively well to the screened correlation coefficient and ratio data. For example, the thin line of screened grid boxes in Africa just south of the equator represents the shift in seasonal fire locations between NH Spring and Summer as it starts in the northern part of southern Africa during NH Spring, and then begins moving south as the season changes to NH Summer. Additionally, the signal shown for South East Asia is representative of the many fires burning each year as the dry season ends and people are clearing their fields.

### **3.3 Regional Time Series of $\text{NH}_3$ , CO, and MODIS Total Fire Counts**

In this Section, the relative emissions of  $\text{NH}_3$  to CO are examined for various fire regions over the entire 13 year data set. This is done by creating a time series plot containing a

monthly average of NH<sub>3</sub> and CO VMR and the Total Monthly MODIS Fire Counts for fire regions of interest. The first four fire regions were selected based off Giglio et al., (2010) and a recent study conducted by Whitburn et al., (2014). The regions “Alaska/CA” and “Russia” were also added. The six regions shown in Figure 9 are; Africa North of the Equator, Africa South of the Equator, Central South America, and South East Asia. The minimum and maximum latitude and longitude values used for each region can be found in Table 1.

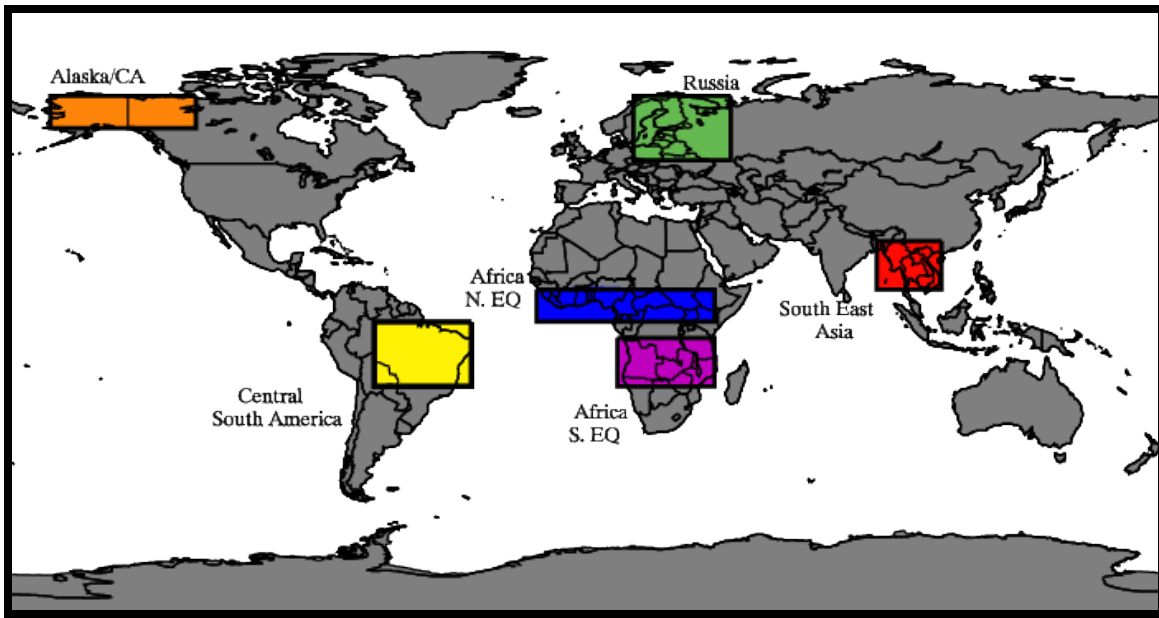


**Figure 9** Map indicating the location of the 6 fire regions to be investigated.

<b>Region</b>	<b>Latitude Min/Max</b>	<b>Longitude Min/Max</b>
<b>Africa North of Equator</b>	0° to 10°N	15° W to 40° E
<b>Africa South of Equator</b>	20° S to 5°S	10° E to 40° E
<b>Central South America</b>	20° S to 0°S	65° W to 35° W
<b>South East Asia</b>	10° N to 25°N	90° E to 110° E
<b>Alaska/CA</b>	60° N to 70° N	165° W to 120° W
<b>Russia</b>	50° N to 60° N	15° E to 45° E

**Table 1.** The minimum and maximum bounding latitude and longitude values for the 6 chosen fire regions of interest.

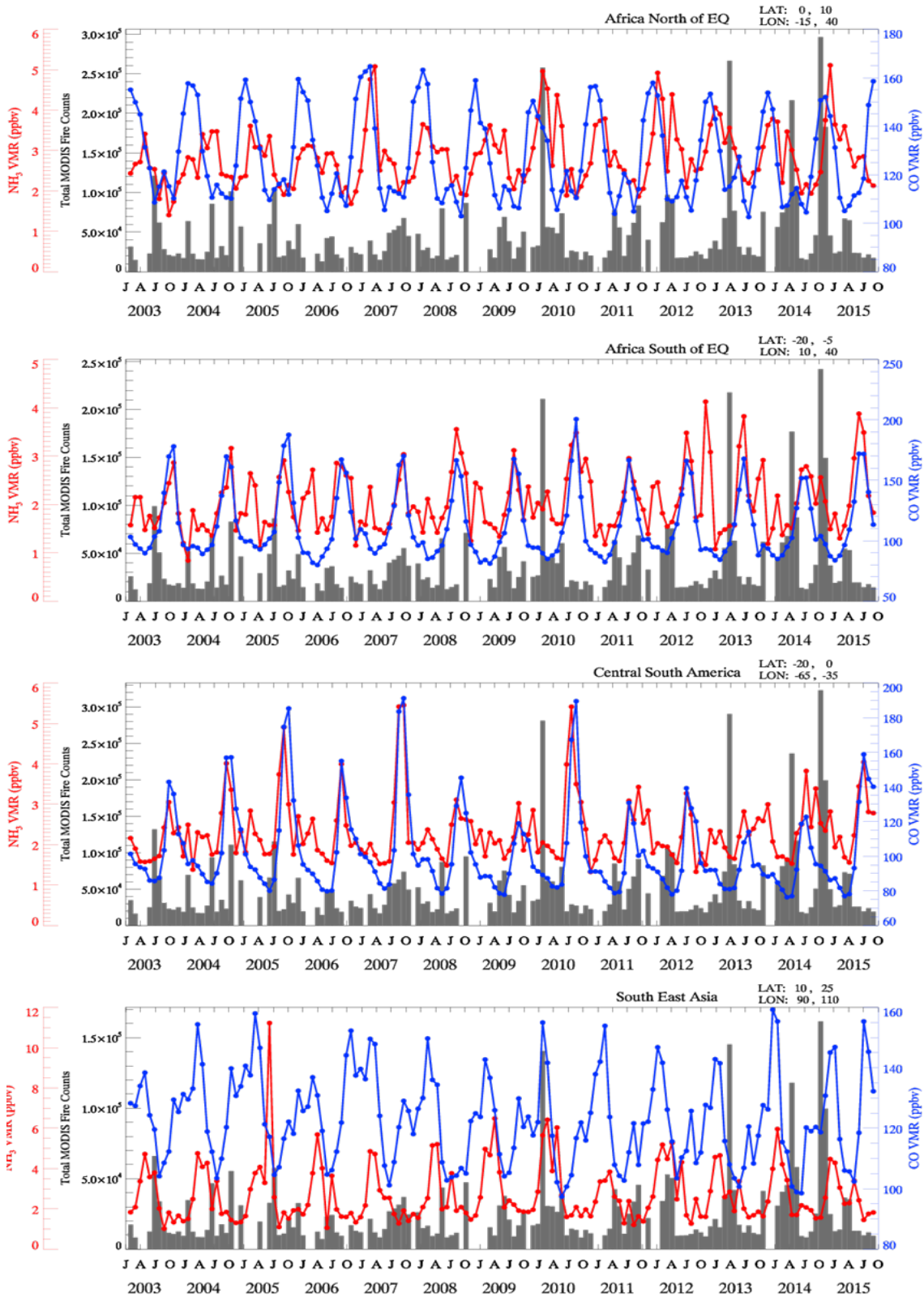


**Figure 10a.** Regional Trends of AIRS NH<sub>3</sub> and CO VMR (ppbv) with Total MODIS Fire Counts for Africa North of the Equator, Africa South of the Equator, Central South America, and South East Asia from 2003-2015. The x-axis is labeled every 3 months (January, April, July, October).



of biomass burning. The primary sources in this region may primarily be anthropogenic such as livestock and other agricultural practices. From all 6 time series, the increased fire activity of 2010 can be seen from the amplified  $\text{NH}_3$  and CO peaks.

### **Chapter 3. Conclusions & Summary**

The primary purpose of this study was to investigate the relationship between  $\text{NH}_3$  and CO emissions from fires in different regions, over various vegetation/land types, and how these differences change over seasonal and decadal time scales using 13 years of satellite measurements from AIRS. By looking at the global distribution of  $\text{NH}_3$  and CO VMR from 2003-2015 we showed that there is a seasonal cycle in both the Northern and Southern Hemisphere. In the Northern Hemisphere the  $\text{NH}_3$  and CO peaks are more pronounced due to industrialization, higher populations, and therefore more agriculture practices. In the Southern Hemisphere the peaks are less pronounced and largely determined by biomass burning activity.

Seasonal correlations of  $\text{NH}_3$  vs CO and  $\text{NH}_3$  to CO relative emission ratios show that, for most cases, positive correlation indicates regions of biomass burning while negative correlation indicates regions of agricultural practices. After determining a “threshold” of correlation coefficient  $> 0.6$ , comparisons of the screened correlation and emission ratios to MODIS Total Fire Counts and Fire Radiative Power confirm the “thresholds” ability to help separate true fire regions. Further examination of the time series of  $\text{NH}_3$  and CO VMR with MODIS Fire Counts of 6 selected fire regions demonstrated the expected agreement between peaks in concentrations and fires.

To more completely understand the relationship between  $\text{NH}_3$  and CO emissions from fires an in-depth study incorporating emission factors from different vegetation and land types is necessary. Although this study has provided significant insight to biomass burning “hot spot” identification there is still much to be considered, particularly for cases where it is difficult to differentiate the sources of  $\text{NH}_3$  and CO emissions.

## References

Abbatt, J. P. D., Benz, S., Cziczo, D. J., Kanji, Z., Lohmann, U. and Mohler, O.: Solid Ammonium Sulfate Aerosols as Ice Nuclei: A Pathway for Cirrus Cloud Formation, *Science* (80-. ), 313(September), 1770–1773, 2006.

Adams, P. J., Seinfeld, J. H., Koch, D., Mickley, L. and Jacob, D.: General circulation model assessment of direct radiative forcing by the sulfate-nitrate-ammonium-water inorganic aerosol system, *J. Geophys. Res. Atmos.*, 106(1), 1097–1111, doi:10.1029/2000JD900512, 2001.

Akagi, S. K., Yokelson, R. J., Wiedinmyer, C., Alvarado, M. J., Reid, J. S., Karl, T., Crouse, J. D. and Wennberg, P. O.: Emission factors for open and domestic biomass burning for use in atmospheric models, *Atmos. Chem. Phys.*, 11(9), 4039–4072, doi:10.5194/acp-11-4039-2011, 2011.

Aneja, V. P., Roelle, P. A., Murray, G. C., Southerland, J., Erisman, J. W., Fowler, D., Asman, W. A. H. and Patni, N.: Atmospheric nitrogen compounds. II: Emissions, transport, transformation, deposition and assessment, *Atmos. Environ.*, 35(11), 1903–1911, doi:10.1016/S1352-2310(00)00543-4, 2001.

Aneja, V. P., Schlesinger, W. H. and Erisman, J. W.: Farming pollution, *Nat. Geosci.*, 1(7), 409–411, doi:10.1038/ngeo236, 2008.

Aumann, H. H., Chahine, M. T., Gautier, C., Goldberg, M. D., Kalnay, E., McMillin, L. M., Revercomb, H., Rosenkranz, P. W., Smith, W. L., Staelin, D. H., Strow, L. L. and Susskind, J.: AIRS/AMSU/HSB on the aqua mission: Design, science objectives, data products, and processing systems, *IEEE Trans. Geosci. Remote Sens.*, 41(2 PART 1), 253–263, doi:10.1109/TGRS.2002.808356, 2003.

Aumann, H. H. H. and Miller, C. R. C.: Atmospheric infrared sounder (AIRS) on the Earth Observing System, *Proc. SPIE*, 2583(December 15, 1995), 332–343, doi:10.1117/12.228579, 1995.

Badr, O. and Probert, S. D.: Carbon monoxide concentration in the Earth's atmosphere, *Appl. Energy*, 49(2), 99–143, doi:10.1016/0306-2619(94)90035-3, 1994.

Beer, R., Shephard, M. W., Kulawik, S. S., Clough, S. A., Eldering, A., Bowman, K. W., Sander, S. P., Fisher, B. M., Payne, V. H., Luo, M., Osterman, G. B. and Worden, J. R.: First satellite observations of lower tropospheric ammonia and methanol, *Geophys. Res. Lett.*, 35(9), 1–5, doi:10.1029/2008GL033642, 2008.

Behera, S. N. and Sharma, M.: Investigating the potential role of ammonia in ion chemistry of fine particulate matter formation for an urban environment, *Sci. Total Environ.*, 408(17), 3569–3575, doi:10.1016/j.scitotenv.2010.04.017, 2010.

- Behera, S. N. and Sharma, M.: Transformation of atmospheric ammonia and acid gases into components of PM<sub>2.5</sub>: An environmental chamber study, *Environ. Sci. Pollut. Res.*, 19(4), 1187–1197, doi:10.1007/s11356-011-0635-9, 2012.
- Bey, I., Jacob, D. J., Yantosca, R. M., Logan, J. A., Field, B. D., Fiore, A. M., Li, Q.-B., Liu, H.-Y., Mickley, L. J. and Schultz, M. G.: Global Modeling of Tropospheric Chemistry with Assimilated Meteorology: Model Description and Evaluation, *J. Geophys. Res.*, 106, 73–95, doi:10.1029/2001JD000807, 2001.
- Brook, R. D., Rajagopalan, S., Pope, C. A., Brook, J. R., Bhatnagar, A., Diez-Roux, A. V., Holguin, F., Hong, Y., Luepker, R. V., Mittleman, M. A., Peters, A., Siscovick, D., Smith, S. C., Whitsett, L. and Kaufman, J. D.: Particulate matter air pollution and cardiovascular disease: An update to the scientific statement from the American Heart Association, *Circulation*, 121(21), 2331–2378, doi:10.1161/CIR.0b013e3181dbee1, 2010.
- Clarisse, L., Clerbaux, C., Dentener, F., Hurtmans, D. and Coheur, P.-F.: Global ammonia distribution derived from infrared satellite observations, *Nat. Geosci.*, 2(7), 479–483, doi:10.1038/ngeo551, 2009.
- Clarisse, L., Shephard, M. W., Dentener, F., Hurtmans, D., Cady-Pereira, K., Karagulian, F., Van Damme, M., Clerbaux, C. and Coheur, P. F.: Satellite monitoring of ammonia: A case study of the San Joaquin Valley, *J. Geophys. Res.*, 115, doi:10.1029/2009jd013291, 2010.
- Coheur, P.-F., Clarisse, L., Turquety, S., Hurtmans, D. and Clerbaux, C.: IASI measurements of reactive trace species in biomass burning plumes, *Atmos. Chem. Phys. Discuss.*, 9(2), 8757–8789, doi:10.5194/acpd-9-8757-2009, 2009.
- Crutzen, P. J., Heidt, L. E., Krasnec, J. P., Pollock, W. H. and Seiler, W.: Biomass burning as a source of atmospheric gases CO, H<sub>2</sub>, N<sub>2</sub>O, NO, CH<sub>3</sub>Cl and COS, *Nature*, 282(5736), 253–256, doi:10.1038/282253a0, 1979.
- Van Damme, M., Clarisse, L., Heald, C. L., Hurtmans, D., Ngadi, Y., Clerbaux, C., Dolman, A. J., Erisman, J. W. and Coheur, P. F.: Global distributions, time series and error characterization of atmospheric ammonia (NH<sub>3</sub>) from IASI satellite observations, *Atmos. Chem. Phys.*, 14(6), 2905–2922, doi:10.5194/acp-14-2905-2014, 2014.
- Van Damme, M., Clarisse, L., Dammers, E., Liu, X., Nowak, J. B., Clerbaux, C., Flechard, C. R., Galy-Lacaux, C., Xu, W., Neuman, J. A., Tang, Y. S., Sutton, M. A., Erisman, J. W. and Coheur, P. F.: Towards validation of ammonia (NH<sub>3</sub>) measurements from the IASI satellite, *Atmos. Meas. Tech.*, 8(3), 1575–1591, doi:10.5194/amt-8-1575-2015, 2015.
- Demarest, P., Richon, K. V. and Wright, F.: Analysis for Monitoring the Earth Science Afternoon Constellation, in AAS/AIAA Astrodynamic Specialist Conference, p. AAS 05-368., 2005.

Fowler, D., Coyle, M., Skiba, U., Sutton, M. A., Cape, J. N., Reis, S., Sheppard, L. J., Jenkins, A., Grizzetti, B., Galloway, N., Vitousek, P., Leach, A., Bouwman, A. F., Butterbach-bahl, K., Dentener, F., Stevenson, D., Amann, M., Voss, M. and Fowler, D.: The global nitrogen cycle in the twenty- first century, *Phil. Trans. R. Soc. B*, 368(2621), 2013.

Galloway, J. N., Townsend, A. R., Erisman, J. W., Bekunda, M., Cai, Z., Freney, J. R., Martinelli, L. A., Seitzinger, S. P. and Sutton, M. A.: Transformation of the Nitrogen Cycle: Recent trends, questions, and potential solutions, *Science* (80-. ), 320, 889–893, 2008.

Giglio, L.: MODIS Collection 6 Active Fire Product User's Guide Revision A. [online] Available from: [http://modis-fire.umd.edu/files/MODIS\\_C6\\_Fire\\_User\\_Guide\\_A.pdf](http://modis-fire.umd.edu/files/MODIS_C6_Fire_User_Guide_A.pdf), 2015.

Giglio, L., van der Werf, G. R., Randerson, J. T., Collatz, G. J. and Kasibhatla, P.: Global estimation of burned area using MODIS active fire observations, *Atmos. Chem. Phys. Discuss.*, 5(6), 11091–11141, doi:10.5194/acpd-5-11091-2005, 2006.

Giglio, L., Randerson, J. T., Van Der Werf, G. R., Kasibhatla, P. S., Collatz, G. J., Morton, D. C. and Defries, R. S.: Assessing variability and long-term trends in burned area by merging multiple satellite fire products, *Biogeosciences*, 7(2008), 1171–1186, doi:10.5194/bg-7-1171-2010, 2010.

Giglio, L., Schroeder, W. and Justice, C. O.: The collection 6 MODIS active fire detection algorithm and fire products, *Remote Sens. Environ.*, 178, 31–41, doi:10.1016/j.rse.2016.02.054, 2016.

Heald, C. L., Collett, J. L., Lee, T., Benedict, K. B., Schwandner, F. M., Li, Y., Clarisse, L., Hurtmans, D. R., Van Damme, M., Clerbaux, C., Coheur, P. F., Philip, S., Martin, R. V. and Pye, H. O. T.: Atmospheric ammonia and particulate inorganic nitrogen over the United States, *Atmos. Chem. Phys.*, 12(21), 10295–10312, doi:10.5194/acp-12-10295-2012, 2012.

IPCC: Anthropogenic and Natural Radiative Forcing., 2013.

Justice, C. O., Giglio, L., Korontzi, S., Owens, J., Morisette, J. T., Roy, D., Descloitres, J., Alleaume, S., Petitcolin, F. and Kaufman, Y.: The MODIS fire products, *Remote Sens. Environ.*, 83(1–2), 244–262, doi:10.1016/S0034-4257(02)00076-7, 2002.

Langridge, J. M., Lack, D., Brock, C. A., Bahreini, R., Middlebrook, A. M., Neuman, J. A., Nowak, J. B., Perring, A. E., Schwarz, J. P., Spackman, J. R., Holloway, J. S., Pollack, I. B., Ryerson, T. B., Roberts, J. M., Warneke, C., De Gouw, J. A., Trainer, M. K. and Murphy, D. M.: Evolution of aerosol properties impacting visibility and direct climate forcing in an ammonia-rich urban environment, *J. Geophys. Res. Atmos.*, 117(6), 1–17, doi:10.1029/2011JD017116, 2012.

Luo, M., Shephard, M. W., Cady-Pereira, K. E., Henze, D. K., Zhu, L., Bash, J. O.,

Pinder, R. W., Capps, S. L., Walker, J. T. and Jones, M. R.: Satellite observations of tropospheric ammonia and carbon monoxide: Global distributions, regional correlations and comparisons to model simulations, *Atmos. Environ.*, 106, 262–277, doi:10.1016/j.atmosenv.2015.02.007, 2015.

NASA: EOS Science Plan: The State of Science in the EOS Program., 1999.

Pinder, R. W., Adams, P. J., Pandis, S. N. and Gilliland, A. B.: Temporally resolved ammonia emission inventories: Current estimates, evaluation tools, and measurement needs, *J. Geophys. Res. Atmos.*, 111(16), 1–14, doi:10.1029/2005JD006603, 2006.

Pope, C. A. and Dockery, D. W.: Health Effects of Fine Particulate Air Pollution: Lines that Connect, *J. Air Waste Manage. Assoc.*, 56(6), 709–742, 2006.

Pope, C. A., Brook, R. D., Burnett, R. T. and Dockery, D. W.: How is cardiovascular disease mortality risk affected by duration and intensity of fine particulate matter exposure? An integration of the epidemiologic evidence, *Air Qual. Atmos. Heal.*, 4(1), 5–14, doi:10.1007/s11869-010-0082-7, 2011.

R'Honi, Y., Clarisse, L., Clerbaux, C., Hurtmans, D., Duflot, V., Turquety, S., Ngadi, Y. and Coheur, P. F.: Exceptional emissions of NH<sub>3</sub> and HCOOH in the 2010 Russian wildfires, *Atmos. Chem. Phys.*, 13(1), 4171–4181, doi:10.5194/acp-13-4171-2013, 2013.

Schoeberl, M. R., Douglass, A. R., Hilsenrath, E., Bhartia, P. K., Barnett, J., Gille, J., Beer, R., Gunson, M., Walters, J., Levelt, P. F. and DeCola, P.: Earth Observing System Missions Benefit Atmospheric Research, *EOS Trans. AGU*, 85(18), 177–181, 2004.

Shephard, M. W. and Cady-Pereira, K. E.: Cross-track Infrared Sounder (CrIS) satellite observations of tropospheric ammonia, *Atmos. Meas. Tech.*, 8(3), 1323–1336, doi:10.5194/amt-8-1323-2015, 2015.

Shephard, M. W., Cady-Pereira, K. E., Luo, M., Henze, D. K., Pinder, R. W., Walker, J. T., Rinsland, C. P., Bash, J. O., Zhu, L., Payne, V. H. and Clarisse, L.: TES ammonia retrieval strategy and global observations of the spatial and seasonal variability of ammonia, *Atmos. Chem. Phys.*, 11(20), 10743–10763, doi:10.5194/acp-11-10743-2011, 2011.

Shukla, S. P. and Sharma, M.: Neutralization of rainwater acidity at Kanpur, India, *Tellus, Ser. B Chem. Phys. Meteorol.*, 62(3), 172–180, doi:10.1111/j.1600-0889.2010.00454.x, 2010.

Susskind, J., Barnet, C. D. and Blaisdell, J. M.: Retrieval of Atmospheric and Surface Parameters From AIRS / AMSU / HSB Data in the Presence of Clouds, *IEEE Trans. Geosci. Remote Sens.*, 41(2), 390–409, doi:10.1109/TGRS.2002.808236, 2003.

Sutton, M. A., Erisman, J. W., Dentener, F. and Möller, D.: Ammonia in the environment: From ancient times to the present, *Environ. Pollut.*, 156(3), 583–604, doi:10.1016/j.envpol.2008.03.013, 2008.

Updyke, K. M., Nguyen, T. B. and Nizkorodov, S. A.: Formation of brown carbon via reactions of ammonia with secondary organic aerosols from biogenic and anthropogenic precursors, *Atmos. Environ.*, 63, 22–31, doi:10.1016/j.atmosenv.2012.09.012, 2012.

Walker, J. M., Philip, S., Martin, R. V. and Seinfeld, J. H.: Simulation of nitrate, sulfate, and ammonium aerosols over the United States, *Atmos. Chem. Phys.*, 12(22), 11213–11227, doi:10.5194/acp-12-11213-2012, 2011.

Warner, J., Carminati, F., Wei, Z., Lahoz, W. and Attié, J. L.: Tropospheric carbon monoxide variability from AIRS under clear and cloudy conditions, *Atmos. Chem. Phys.*, 13(24), 12469–12479, doi:10.5194/acp-13-12469-2013, 2013.

Warner, J. X., Wei, Z., Strow, L. L., Barnet, C. D., Sparling, L. C., Diskin, G. and Sachse, G.: Improved agreement of AIRS tropospheric carbon monoxide products with other EOS sensors using optimal estimation retrievals, *Atmos. Chem. Phys.*, 10(19), 9521–9533, doi:10.5194/acp-10-9521-2010, 2010.

Warner, J. X., Wei, Z., Larrabee Strow, L., Dickerson, R. R. and Nowak, J. B.: The global tropospheric ammonia distribution as seen in the 13-year AIRS measurement record, *Atmos. Chem. Phys.*, 16(8), 5467–5479, doi:10.5194/acp-16-5467-2016, 2016.

van der Werf, G. R., Randerson, J. T., Giglio, L., Collatz, G. J., Kasibhatla, P. S. and Arellano, A. F., J.: Interannual variability in global biomass burning emissions from 1997 to 2004, *Atmos. Chem. Phys.*, 6(11), 3423–3441, doi:10.5194/acpd-6-3175-2006, 2006.

Whitburn, S., Van Damme, M., Kaiser, J. W., Van Der Werf, G. R., Turquety, S., Hurtmans, D., Clarisse, L., Clerbaux, C. and Coheur, P. F.: Ammonia emissions in tropical biomass burning regions: Comparison between satellite-derived emissions and bottom-up fire inventories, *Atmos. Environ.*, 121, 42–54, doi:10.1016/j.atmosenv.2015.03.015, 2014.

Wooster, M. J., Roberts, G., Perry, G. L. W. and Kaufman, Y. J.: Retrieval of biomass combustion rates and totals from fire radiative power observations: FRP derivation and calibration relationships between biomass consumption and fire radiative energy release, *J. Geophys. Res. Atmos.*, 110(24), 1–24, doi:10.1029/2005JD006318, 2005.